Suppression of Injection Voltage Disturbance for High Frequency Square-Wave Injection Sensorless Drive with Regulation of Induced High Frequency Current Ripple

Dongouk Kim, Yong-Cheol Kwon, and Seung-Ki Sul
School of Electrical & Computer Engineering
Seoul National University
Seoul, Korea
kdw@eepel.snu.ac.kr, dydcjfe@eepel.snu.ac.kr, sulsk@plaza.snu.ac.kr

Jang-Hwan Kim and Rae-Sung Yu
Manufacturing Technology Center
SAMSUNG ELECTRONICS Company, Ltd
Suwon, Korea
janghwane.kim@samsung.com, rs.yu@samsung.com

***Abstract*—In square wave voltage signal injection sensorless drive, the injection voltage can be distorted by the inverter nonlinearity effects especially when the injection voltage is low. If that happens, High Frequency (HF) current signal which contains the rotor position information could be also distorted, which directly leads to an error in the position estimation. This paper analyzes the effects of the inverter nonlinearity to injection voltage, to induced current ripple, and to the position estimation performance in sequence and proposes a voltage injection method to minimize the impact of the inverter nonlinearity by the regulation of HF current ripple. By simulations and experiments, performance of the proposed method has been verified. The experimental results show 34.9% reduction of noise input in the position estimation and 19.7% improvement of the position estimation performance under 15% of rated voltage signal injection**

NOMENCLATURE

Superscript 's'	stationary reference frame.
Superscript 'r'	rotor reference frame.
Superscript '*'	reference value.
θ_r	electrical rotor position.
$\hat{\theta}_r$	estimated value of θ_r.
$\tilde{\theta}_r$	rotor position estimation error, $\theta_r - \hat{\theta}_r$.
T_{sw}, f_{sw}	switching period and frequency.
T_{samp}, f_{samp}	sampling period and frequency.
T_h, f_h	signal injection period and frequency.
L_{ds}, L_{qs}	Synchronous inductances.

I. INTRODUCTION

Sensorless control techniques made it possible to realize accurate estimation of rotor position without additional position sensors. Especially at standstill and low speed, saliency based methods [1]-[5] are normally used. Since the rotor position determines spatial distribution of inductance, it can be estimated by injecting signal and analyzing its response. Through several researches and developments, the saliency based methods have been evolved to be compatible to low end sensored servo drives. The control bandwidth of recently reported square-wave signal injection sensorless drive could extend to 40Hz in the case of speed control loop and 10Hz in the case of position control loop [5].

But additional signal injection causes undesired effects such as acoustic noise, reduced voltage margin of inverter, and losses coming from induced current ripple. These problems can be relieved by reducing injection voltage magnitude, resulting in less induced current ripple. However, the inverter nonlinearity effects would be getting larger as the magnitude of the square wave is getting smaller. Since the inverter nonlinearity effects induce considerable error in the rotor position estimation [6]-[7], it is difficult to reduce the injection voltage under a certain limiting value.

In principle, the inverter nonlinearity effects are mainly determined by the switching sequence (on and off sequences) and phase current at switching instant. In Ref. [8]-[10], several compensation methods had been proposed, where compensation factors were calculated from the sampled current. But due to the time delay from the current sampling to the PWM switching of inverter which is about $1.5 \cdot T_{samp}$ [11], it is inappropriate to use the sampled current for the compensation under the square-wave voltage injection sensorless drive where the current varies rapidly. Ref. [12] proposed a compensation method that was done from the prediction of the current at the switching instant. But this algorithm is vulnerable to the variation of drive system parameters since the prediction depends on the parameters. Accurate prediction of the current at the switching instant during the square-wave injection is almost impossible. In Ref. [13], High Frequency (HF) current ripple coming from signal injection was processed to calculate and feed-forward HF component of voltage distortion. But, this method mainly focused on sinusoidal voltage injection whose frequency was in several hundreds of Hz range where T_h was at least 20 times of T_{samp}. In square-wave voltage injection sensorless drive where T_h is only 2 or 4 times of T_{samp}, feed-forwarding based on sensed and filtered current signal can be inaccurate due to the $1.5 \cdot T_{samp}$ time delay.

This paper proposes a voltage signal injection technique to cope with the degradation of position estimation performance caused by the inverter nonlinearity effects in square-wave signal injection sensorless drive. Contrary to the conventional voltage injection methods [10], the proposed method does not inject voltage with fixed magnitude, but varies the magnitude of the injection voltage to regulate the magnitude of the induced current ripple.. By the regulation, the noise component included in position information can conspicuously decrease under the constraint of the same rms value of the current ripple. In other words, the injection voltage can be decreased without degrading the sensorless control performance. The effectiveness of the proposed method is verified by series of experiments.

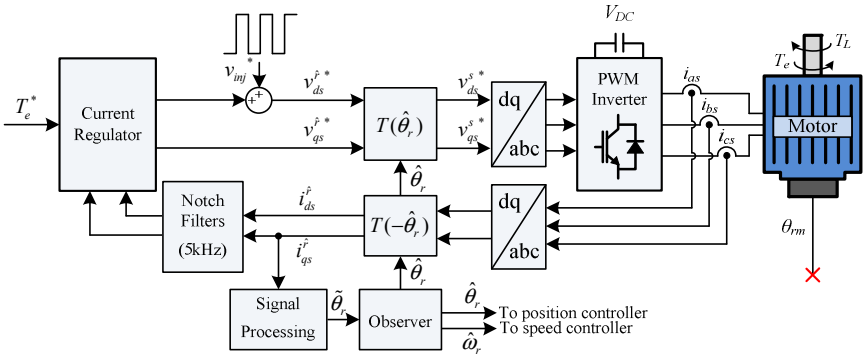

Fig. 1. Block diagram of conventional square-wave voltage injection sensorless control.

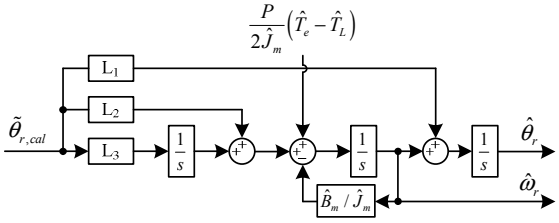

Fig. 2. Position and speed observer based on mechanical model.

II. Position Estimation by Square-Wave Injection

In square-wave injection sensorless control, square-wave voltage expressed as (1) is injected to estimated d-axis as shown in Fig. 1.

$$\begin{bmatrix} v_{dsh}^{\hat{r}} \\ v_{qsh}^{\hat{r}} \end{bmatrix} = \begin{bmatrix} v_{inj}^{\ *} \\ 0 \end{bmatrix}, \text{where } v_{inj}^{\ *} = \begin{cases} V_h, & \text{half duty} \\ -V_h, & \text{otherwise} \end{cases} \quad (1)$$

Then the injection voltage in real rotor reference frame can be deduced as (2).

$$\begin{bmatrix} v_{dsh}^{r} \\ v_{qsh}^{r} \end{bmatrix} = T_{\tilde{\theta}_r} \begin{bmatrix} v_{dsh}^{\hat{r}} \\ v_{qsh}^{\hat{r}} \end{bmatrix} = \begin{bmatrix} \cos\tilde{\theta}_r & \sin\tilde{\theta}_r \\ -\sin\tilde{\theta}_r & \cos\tilde{\theta}_r \end{bmatrix} \begin{bmatrix} v_{inj}^{\ *} \\ 0 \end{bmatrix} = \begin{bmatrix} v_{inj}\cos\tilde{\theta}_r \\ -v_{inj}\sin\tilde{\theta}_r \end{bmatrix}. \quad (2)$$

And current ripple induced by injection voltage in estimated rotor reference frame can be calculated by (3)-(4).

$$\begin{bmatrix} \Delta i_{dsh}^{r} \\ \Delta i_{qsh}^{r} \end{bmatrix} = \int_{t}^{t+T_{samp}} \begin{bmatrix} L_{ds} & 0 \\ 0 & L_{qs} \end{bmatrix}^{-1} \begin{bmatrix} v_{dsh}^{r} \\ v_{qsh}^{r} \end{bmatrix} d\tau = T_{samp} \begin{bmatrix} \frac{1}{L_{ds}}\cos\tilde{\theta}_r \cdot v_{inj}^{\ *} \\ -\frac{1}{L_{qs}}\sin\tilde{\theta}_r \cdot v_{inj}^{\ *} \end{bmatrix}. \quad (3)$$

$$\begin{bmatrix} \Delta i_{dsh}^{\hat{r}} \\ \Delta i_{qsh}^{\hat{r}} \end{bmatrix} = T_{\tilde{\theta}_r}^{-1} \begin{bmatrix} \Delta i_{dsh}^{r} \\ \Delta i_{qsh}^{r} \end{bmatrix} = T_{samp} \begin{bmatrix} \left(\frac{1}{L_{ds}}\cos^2\tilde{\theta}_r + \frac{1}{L_{qs}}\sin^2\tilde{\theta}_r \right) \cdot v_{inj}^{\ *} \\ \left(\frac{1}{2}\frac{(L_{qs}-L_{ds})}{L_{ds}L_{qs}}\sin 2\tilde{\theta}_r \right) \cdot v_{inj}^{\ *} \end{bmatrix}. \quad (4)$$

From q-axis current ripple in (4), $\tilde{\theta}_r$ can be estimated by (5).

$$\tilde{\theta}_{r,cal} = \Delta i_{qsh}^{\hat{r}} \cdot \frac{L_{ds}L_{qs}}{T_{samp}v_{inj}^{\ *}(L_{qs}-L_{ds})} = \frac{1}{2}\sin 2\tilde{\theta}_r \approx \tilde{\theta}_r. \quad (5)$$

Then, rotor position and speed can be estimated by a PID observer shown in Fig. 2 based on mechanical model using $\tilde{\theta}_{r,cal}$ as an input to the observer. The observer works by eliminating q-axis current ripple which corresponds to the position estimation error.

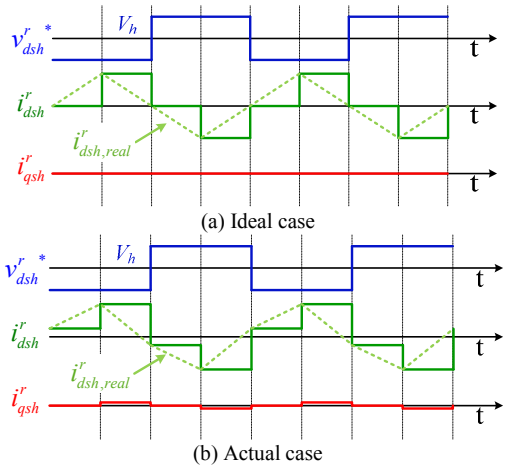

Fig. 3. Distortion of d-axis current ripple during square-wave injection.

III. Distortion of Voltage and Current by Inverter Nonlinearity Effects

The rotor position estimation through (1)-(5) can be deteriorated by the inverter nonlinearity effects. Assume that square-wave voltage with uniform magnitude is injected to actual d-axis. Ideally, d-axis current ripple induced by square-wave voltage must be regular like Fig. 3(a) and there should be no current ripple in q-axis. Note that i_{dsh}^{r} and i_{qsh}^{r} in Fig. 3 are sample and hold waveforms. However, actual experimental current waveforms are different from the ideal ones. In Fig. 3(b), d-axis current ripple waveform is quite distorted and unexpected current ripple appears in q-axis due to the inverter nonlinearity effects. This current ripple in q-axis causes position estimation error, which will be discussed in the next section. Since the position information is extracted from the sensed current ripple, the irregular current ripple can cause position estimation error. This section investigates how the current waveform in Fig. 3(b) is induced by the inverter nonlinearity effects during square-wave voltage injection sensorless drive.

Inverter itself is not completely linear and its output pole voltage may be different from its reference. Pole voltage error from the inverter nonlinearity can be defined as (6).

$$v_{err} = v_{an}^{\ *} - v_{an\_real} \quad (6)$$

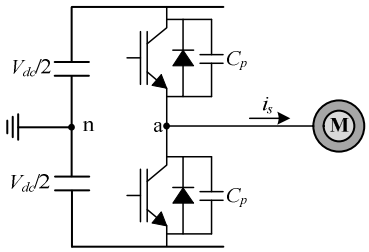

Fig. 4. One phase arm of an inverter feeding a motor.

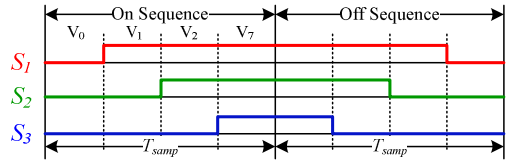

Fig. 5. Gating signals at on and off sequences.

Three main sources of the inverter nonlinearity that cause the voltage error are to be explained one by one.

A. Diode conduction characteristic during dead time [9]

Fig. 4 is a conceptual diagram describing one phase arm of an inverter feeding a motor. In the figure, the phase current denoted as i_s doesn't flow through active switching device during the dead time but only flows through diode. If the current flows to the load during the dead time, the lower diode is turned on. However, if the current flows to inverter, the upper diode is turned on. The voltage distortion by diode conduction characteristic during the dead time is mainly determined by polarity of phase current and switching sequence as expressed in (7), where the dead time is denoted as T_{dead}.

$$v_{err\_DT} = \begin{cases} V_{dc}\dfrac{T_{dead}}{T_{samp}} & (i_s>0,\ \text{on sequence}) \\ 0 & (i_s<0,\ \text{on sequence}) \\ 0 & (i_s>0,\ \text{off sequence}) \\ -V_{dc}\dfrac{T_{dead}}{T_{samp}} & (i_s<0,\ \text{off sequence}) \end{cases} \quad (7)$$

Fig. 5 describes gating signals of each arm during on and off sequences.

B. Parasitic capacitance effect during dead time [14]

If the magnitude of current is near zero during the dead time, the pole voltage is affected by charging and discharging phenomena of the parasitic capacitor denoted as C_p in Fig. 3. Let $i_c(=V_{dc}/T_{dead}\cdot C_{st})$ the critical value of i_s when the dead time is equal to the charging or discharging time of C_p. The pole voltage error induced by parasitic capacitance effect can be expressed as follows.

$$v_{err\_PC} = \begin{cases} -(\dfrac{C_{st}V_{dc}^2}{2T_{samp}})\dfrac{1}{i_s} & (i_s<0,\ |i_s|>|i_c|,\ \text{on sequence}) \\ (V_{dc}+\dfrac{T_{dead}}{2C_{st}}i_s)\dfrac{T_{dead}}{T_{samp}} & (i_s<0,\ |i_s|\le|i_c|,\ \text{on sequence}) \\ -(\dfrac{C_{st}V_{dc}^2}{2T_{samp}})\dfrac{1}{i_s} & (i_s>0,\ |i_s|>|i_c|,\ \text{off sequence}) \\ -(V_{dc}-\dfrac{T_{dead}}{2C_{st}}i_s)\dfrac{T_{dead}}{T_{samp}} & (i_s>0,\ |i_s|\le|i_c|,\ \text{off sequence}) \end{cases} \quad (8)$$

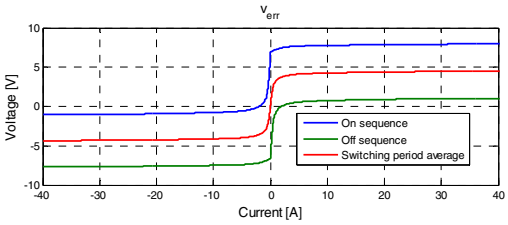

Fig. 6. Pole voltage error by inverter nonlinearity.

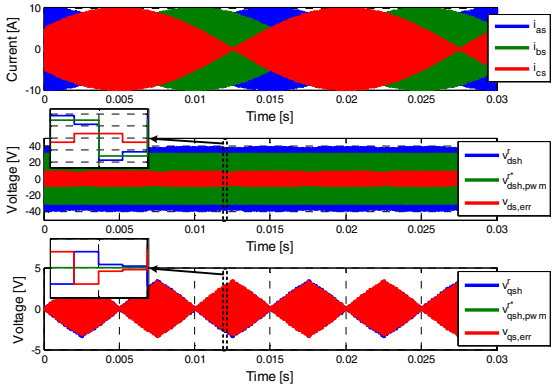

Fig. 7. Voltage distortion in rotor reference frame. (zero DC current, V_h=30V).

C. Voltage drop of switching device

Every semiconductor devices have intrinsic voltage drop when conducting current. The pole voltage error of switching device by the voltage drop can be represented as a function of current flowing through it as expressed in (9).

$$\begin{aligned} v_{err\_Switch} &= g(i_{Switch}) \\ v_{err\_Diode} &= g(i_{Diode}) \end{aligned} \quad (9)$$

Inverter nonlinearity is affected by three main sources aforementioned. The total pole voltage error is the sum of the three error terms, that is

$$v_{err} = v_{err\_DT} + v_{err\_PC} + \frac{v_{err\_Switch} + v_{err\_Diode}}{2}. \quad (10)$$

In (10), duty ratio of the switch is assumed as a half. The total pole voltage error with V_{dc}=144V, T_{dead}=2μs, C_p=5nF, and V-I characteristics from switching device, PM300CL1A060, is shown in Fig. 6.

The voltage error in rotor reference frame, i.e., $v_{ds,err}$ and $v_{qs,err}$, can be calculated through coordinate transformation of pole voltage error in (10). Fig. 7 shows the tendency of d-q voltage error with zero DC current, V_h=30V, f_h=0.5·f_{sw}, f_{samp}=2·f_{sw}. In the figure, $v^r_{dsh} = v^{r*}_{dsh,pwm} - v_{ds,err}$. As shown in Fig. 6, the pole voltage error rapidly varies near zero current. Thus multiple zero crossing of phase current in Fig. 7 induces rapid variation of the voltage error. The waveform of $v_{ds,err}$ is periodic and is synchronized to v^*_{inj} since the current pulsation is in d-axis. And the absolute value of v^r_{dsh} has the frequency of 2·f_h. On the other hand, $v_{qs,err}$ is not synchronized to v^*_{inj} and thus it is difficult to expect the overall waveform of v^r_{qsh}. Although $v_{qs,err}$ is smaller than $v_{ds,err}$ in its magnitude, q-axis current ripple induced by $v_{qs,err}$

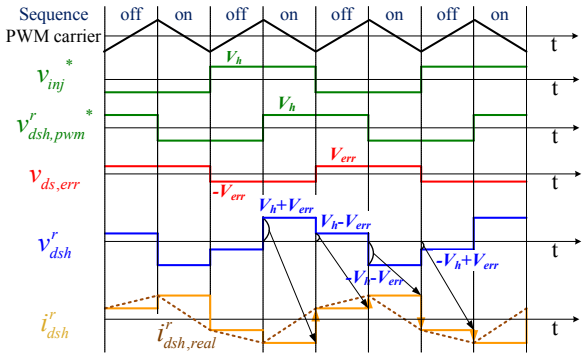

Fig. 8. Step-by-step procedure of current distortion.

significantly causes rotor position estimation error, which will be analyzed in the next section.

From these observations, the current ripple distortion in Fig. 3(b) can be explained by Fig. 8. By the voltage error induced by the inverter nonlinearity effects, the actual injection voltage is distorted and the sampled current waveform like Fig. 3(b) could be generated.

Fig. 9 shows the voltage error with zero DC current, V_h=12V, f_h=0.5·f_{sw}, f_{samp}=2·f_{sw}. In this case, current ripple magnitude decreased from that in Fig. 7 due to reduced injection voltage. However, $v_{ds,err}$ and $v_{qs,err}$ in Fig. 9 are almost the same as that in Fig. 7. This is because the voltage error in Fig. 6 is saturated as the current increases. If the current ripple magnitude is larger than a certain value, $v_{ds,err}$ and $v_{qs,err}$ do not change much. Focusing on the actual injection voltage, $v^r_{dsh,real}$ is more distorted in Fig. 9 than in Fig. 7 since $v^{r\,*}_{dsh}$ is much larger than $v_{ds,err}$ in Fig. 9. $v^r_{qsh,real}$ in Fig. 7 and 9 are almost the same since $v^{r\,*}_{qsh}$ is zero in both cases.

Fig. 10 shows the voltage error with rated current at q-axis, V_h=30V, f_h=0.5·f_{sw}, f_{samp}=2·f_{sw}. In this condition, pulsation occurs in $v_{ds,err}$ only six times per fundamental cycle when a phase current multiply crosses zero. And $v_{qs,err}$ is static without pulsation since there is large DC current without HF ripples in q-axis.

IV. Effects of Current Ripple Distortion on Rotor Position Estimation

Considering the inverter nonlinearity effects, injection voltage terms (1)-(2) can be modified to (11)-(12) where voltage error terms are added.

$$\begin{bmatrix} v^{\hat{r}}_{dsh} \\ v^{\hat{r}}_{qsh} \end{bmatrix} = \begin{bmatrix} v_{inj}^{\,*} - v_{ds,err} \\ -v_{qs,err} \end{bmatrix}. \tag{11}$$

$$\begin{bmatrix} v^{r}_{dsh} \\ v^{r}_{qsh} \end{bmatrix} = \begin{bmatrix} \left(v_{inj}^{\,*} - v_{ds,err}\right)\cos\tilde{\theta}_r - v_{qs,err}\sin\tilde{\theta}_r \\ -\left(v_{inj}^{\,*} - v_{ds,err}\right)\sin\tilde{\theta}_r - v_{qs,err}\cos\tilde{\theta}_r \end{bmatrix}. \tag{12}$$

The current ripple in estimated rotor reference frame can be deduced through (13)-(14).

$$\begin{bmatrix} \Delta i^{r}_{dsh} \\ \Delta i^{r}_{qsh} \end{bmatrix} = T_{samp} \begin{bmatrix} \frac{1}{L_{ds}}\left\{\left(v_{inj}^{\,*} - v_{ds,err}\right)\cos\tilde{\theta}_r - v_{qs,err}\sin\tilde{\theta}_r\right\} \\ \frac{1}{L_{qs}}\left\{-\left(v_{inj}^{\,*} - v_{ds,err}\right)\sin\tilde{\theta}_r - v_{qs,err}\cos\tilde{\theta}_r\right\} \end{bmatrix}. \tag{13}$$

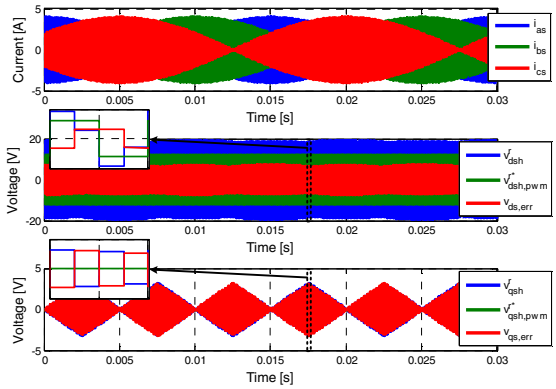

Fig. 9. Voltage distortion in rotor reference frame. (zero DC current, V_h=12V)

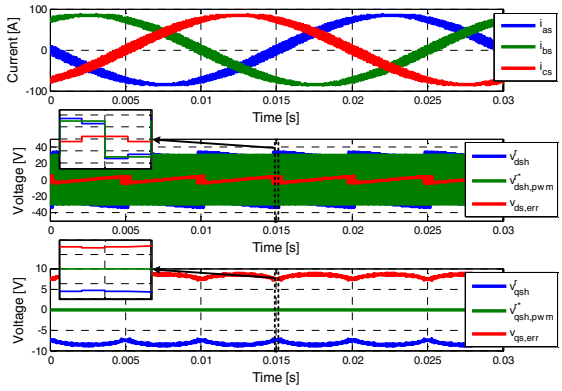

Fig. 10. Voltage distortion in rotor reference frame. (rated current at q-axis, V_h =30V)

$$\begin{aligned} \begin{bmatrix} \Delta i^{\hat{r}}_{dsh} \\ \Delta i^{\hat{r}}_{qsh} \end{bmatrix} &= T_{samp} \begin{bmatrix} \left(\frac{\cos^2\tilde{\theta}_r}{L_{ds}} + \frac{\sin^2\tilde{\theta}_r}{L_{qs}}\right)\cdot\left(v_{inj}^{\,*} - v_{ds,err}\right) \\ -\frac{\sin 2\tilde{\theta}_r}{2}\cdot\frac{L_{qs}-L_{ds}}{L_{ds}L_{qs}}\cdot v_{qs,err} \\ \frac{\sin 2\tilde{\theta}_r}{2}\cdot\frac{L_{qs}-L_{ds}}{L_{ds}L_{qs}}\cdot\left(v_{inj}^{\,*} - v_{ds,err}\right) \\ -\left(\frac{\sin^2\tilde{\theta}_r}{L_{ds}} + \frac{\cos^2\tilde{\theta}_r}{L_{qs}}\right)\cdot v_{qs,err} \end{bmatrix} \\ &\approx T_{samp} \begin{bmatrix} -\frac{L_{qs}-L_{ds}}{L_{ds}L_{qs}}\cdot v_{qs,err}\cdot\tilde{\theta}_r + \frac{v_{inj}^{\,*} - v_{ds,err}}{L_{ds}} \\ \frac{L_{qs}-L_{ds}}{L_{ds}L_{qs}}\cdot\left(v_{inj}^{\,*} - v_{ds,err}\right)\cdot\tilde{\theta}_r - \frac{v_{qs,err}}{L_{qs}} \end{bmatrix}. \end{aligned} \tag{14}$$

In (14), $v_{ds,err}$ and $v_{qs,err}$ appear in q-axis current ripple that is necessary signal to estimate rotor position. Applying the computation in (5), the extracted signal becomes as follows.

$$\begin{aligned} &\tilde{\theta}_{r,cal} \approx k_{scale}\cdot\tilde{\theta}_r + N, \\ &\text{where} \begin{cases} k_{scale} = 1 - \dfrac{v_{ds,err}}{v_{inj}^{\,*}} \\ N = -\dfrac{L_{ds}v_{qs,err}}{v_{inj}^{\,*}(L_{qs}-L_{ds})} \end{cases}. \end{aligned} \tag{15}$$

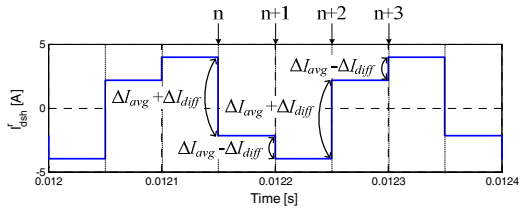

Fig. 11. d-axis current ripple waveform. (zero DC current, V_h =12V)

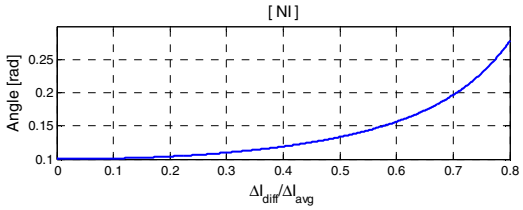

Fig. 12. Noise index according to $\Delta I_{diff}/\Delta I_{avg}$.

In (15), the first term related with $\tilde{\theta}_r$ is an effective signal that helps the position estimation and the second term works as a noise input denoted as n in Fig. 2. Due to the inverter nonlinearity effects, k_{scale} is not the unity but fluctuates as $v_{ds,err}$ pulsates. This is equivalent to the fluctuation of observer gains, L_1-L_3, which significantly degrades the position estimation performance. And the noise term denoted as n generated by $v_{qs,err}$ directly leads to position estimation error. Since v_{inj}^* is a square-wave signal with frequency f_h, only AC signal of $v_{qs,err}$ with frequency f_h works as a noise input. In the case of Fig. 9 when the injection voltage is low, both k_{scale} and N increase, which means more fluctuation observer gains and more noise input to the observer. This is why the position estimation performance is degraded when the injection voltage is low. In the case of Fig. 10, large DC value in $v_{qs,err}$ is filtered out and does not contribute to the noise input. For this reason, the position estimation performance is less influenced by the inverter nonlinearity effects in load condition.

V. Proposed Voltage Injection Method

Rearranging the d-axis equation in (14), v_{inj}^* can be expressed as (16).

$$v_{inj}^* \approx \frac{L_{ds}}{T_{samp}}\Delta i_{dsh}^{\hat{r}} + \frac{L_{qs}-L_{ds}}{L_{qs}}\cdot v_{qs,err}\cdot\tilde{\theta}_r + v_{ds,err}. \quad (16)$$

Substituting (16) into the q-axis equation in (14), q-axis current ripple can be expressed as a function of $\Delta i_{dsh}^{\hat{r}}$ and $v_{qs,err}$.

$$\Delta i_{qsh}^{\hat{r}} \approx \frac{L_{qs}-L_{ds}}{L_{qs}}\cdot\Delta i_{dsh}^{\hat{r}}\cdot\tilde{\theta}_r - \Delta i_{qsh,err}. \quad (17)$$

$\Delta i_{qsh,err}$ in (17) indicates $T_{samp}/L_{qs}\cdot v_{qs,err}^r$ which is the ripple component induced by q-axis voltage distortion. In (17), the effective term is proportional to $\Delta i_{dsh}^{\hat{r}}$. Then the computation of $\tilde{\theta}_{r,cal}$ can be improved by (18).

$$\tilde{\theta}_{r,cal} = \Delta i_{qsh}^{\hat{r}}\cdot\frac{L_{qs}}{\left(L_{qs}-L_{ds}\right)\Delta i_{dsh}^{\hat{r}}} \approx \tilde{\theta}_r - \frac{L_{qs}}{\left(L_{qs}-L_{ds}\right)}\cdot\frac{\Delta i_{qsh,err}}{\Delta i_{dsh}^{\hat{r}}}. \quad (18)$$

Dividing $\Delta i_{qsh}^{\hat{r}}$ by $\Delta i_{dsh}^{\hat{r}}$ and inductance terms, the fluctuation of observer gains can be suppressed since k_{scale} becomes the unity in (18). From the last term in (18) a Noise Index (NI) can be defined as (19).

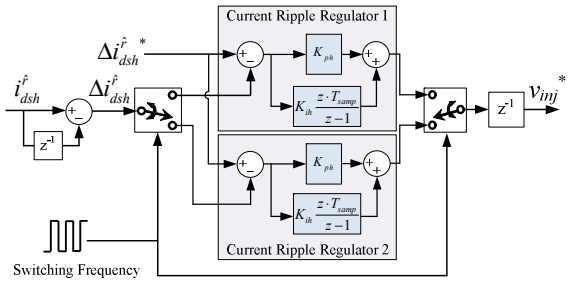

Fig. 13. Block diagram of proposed scheme.

$$\mathrm{NI} = \frac{\Delta i_{qsh,err}}{\Delta i_{dsh}^{\hat{r}}}. \quad (19)$$

NI is the source of the noise input to the observer in Fig. 2.

The key idea of the proposed algorithm is to reduce NI by regulating $\left|\Delta i_{dsh}^{\hat{r}}\right|$. By regulating the magnitude of $\Delta i_{dsh}^{\hat{r}}$, NI can be reduced in the moving average sense. For example, the waveform of $\Delta i_{dsh}^{\hat{r}}$ in the same condition as Fig. 9 is shown in Fig. 11. The magnitude of $\Delta i_{dsh}^{\hat{r}}$ can be expressed as (20).

$$\left|\Delta i_{dsh}^{\hat{r}}\right| = \Delta I_{avg} + (-1)^n\,\Delta I_{diff}, \quad (20)$$

where n means sampling count. For constant magnitude of $\Delta i_{dsh}^{\hat{r}}$ like the case in Fig. 3(a), ΔI_{diff} would be zero. ΔI_{diff} becomes larger with low injection voltage like the case of Fig. 11 because the magnitude of $v_{ds,err}$ is comparable to V_h. Assume that

$$\left|\Delta i_{qsh}^{\hat{r}}\right| = k\cdot\Delta I_{avg}. \quad (21)$$

Then the moving average of NI for two sampling periods can be calculated as

$$[\mathrm{NI}] = \frac{k}{1-\left(\Delta I_{diff}/\Delta I_{avg}\right)^2}. \quad (22)$$

With k=0.1, the moving average of NI is shown in Fig. 12. In Fig. 11 $\Delta I_{diff}/\Delta I_{avg}$=0.541 and [NI]=0.141. If $\Delta i_{dsh}^{\hat{r}}$ is regulated, ΔI_{diff} becomes zero and [NI]=0.1. By the regulation of $\Delta i_{dsh}^{\hat{r}}$, the noise input can be reduced by 29.1% under the constraint of the same peak-to-peak current ripple. The effect of constant $\Delta i_{dsh}^{\hat{r}}$ becomes larger with lower injection voltage, i.e., smaller magnitude of V_h.

Fig. 13 shows the implementation of the current ripple regulation. Instead of injecting pulsating voltage with fixed magnitude in Fig. 1, the injection voltage is adjusted by PI regulator in order to fix the magnitude of $\Delta i_{dsh}^{\hat{r}}$. There are two current ripple regulators work together alternately. Because $\Delta i_{dsh}^{\hat{r}}$ has the same magnitude for every other sampling instant as shown in Fig. 11, one regulator can be used for even sampling instants and the other can be used for odd sampling instants.

$$\begin{aligned}\left|\Delta i_{dsh}^{\hat{r}}\right|[\mathrm{n}] &= \left|\Delta i_{dsh}^{\hat{r}}\right|[\mathrm{n}+2] \\ &\neq \left|\Delta i_{dsh}^{\hat{r}}\right|[\mathrm{n}+1].\end{aligned} \quad (23)$$

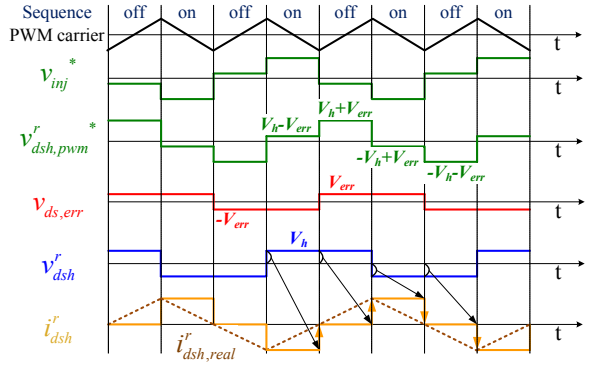

Fig. 14. Procedure of current ripple regulation.

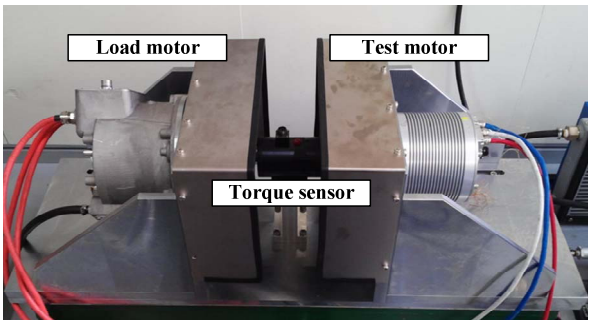

Fig. 15. Experimental setup.

Fig. 14 shows how Δi_{dsh}^r is regulated by the proposed scheme. In the steady state, the current ripple is regulated, which means that the actual injection voltage has the waveform as shown in Fig. 14. In other words, $v_{ds,err}$ can be completely compensated by the proposed scheme.

VI. Experimental Results

The hardware platform to evaluate the proposed scheme is constructed based on a TMS28335 DSP. The power devices used in prototype inverter is MITSUBISHI PM300CAL1A06 IPM. f_{sw}=10kHz, f_{samp}=20kHz, f_h=5kHz, V_{dc}=144V, and T_{dead} is set as 2μs. Fig. 15 shows experimental setup. The target motor on the right side of the test bed is IPMSM whose parameters are specified in Table I.

TABLE I. Parameters of IPMSM

IPMSM Parameter	Value
Rated power	8 kW
Rated current	60 A_{rms}
Pole number	10
Back-EMF constant	0.0281 V·s
Winding resistance	0.01 Ω
Synchronous inductances	L_{ds}: 143 μH, L_{qs}: 216 μH

A. Regulation of HF Current Ripple

Fig. 16 shows the regulation of HF current ripple by the proposed scheme. Using conventional voltage injection method, the waveform of i_{dsh}^r is irregular due to the inverter nonlinearity effects. Applying the proposed voltage injection method, i_{dsh}^r is kept regular thanks to adjusted v_{inj}^* as shown in Fig. 16(b).

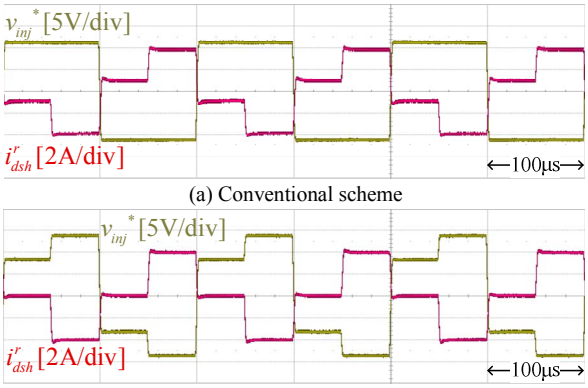

Fig. 16. Experiment A: Injection voltage and current ripple.

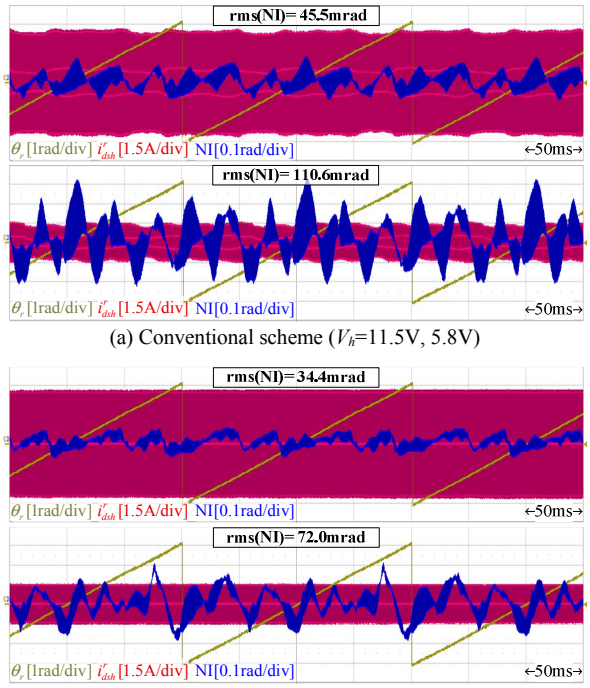

Fig. 17. Experiment B: Measurement of NI. (60r/min, zero current)

B. Reduction of Noise Index

The noise index defined in (19) can be experimentally measured. Under sensored operation, $\tilde{\theta}_r$ is equal to zero. In this condition, q-axis current ripple is induced only by the inverter nonlinearity effects, that is $\Delta i_{qsh}^r = \Delta i_{qsh,err}$. Dividing Δi_{qsh}^r by Δi_{dsh}^r, NI can be calculated.

Fig. 17 shows experimental waveforms of noise indices in no load condition. In the figure, rms values of the current ripples are matched for fair comparison considering the losses and acoustic noises. V_h=11.5V and 5.8V correspond to $|\Delta i_{dsh}^{r*}|$ = 4A and 1.41A, respectively. It is evident in the figure that noise indices are conspicuously attenuated by the proposed voltage injection technique. In the three cases, the percentages of NI reduction are 24.4% and 34.9%.

Fig. 18 shows the same noise index waveforms in full load condition. Thanks to reduced number of zero crossings of phase currents in this condition, the inverter nonlinearity effects are smaller. Comparing Fig. 17(a) and Fig. 18(a), it can be known that although the injection voltage is not

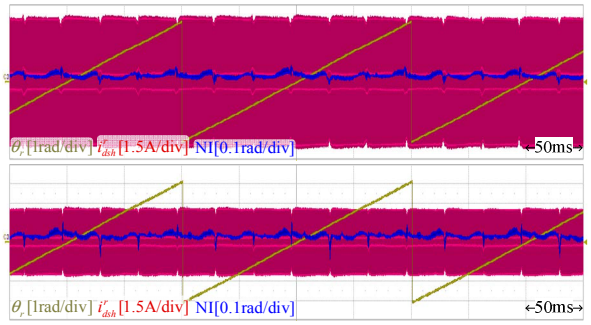

(a) Conventional scheme (V_h=11.5V, 5.8V)

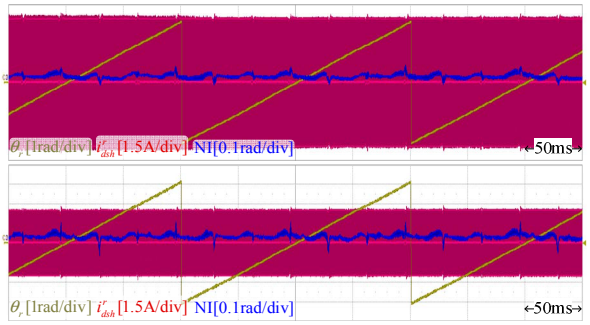

(b) Proposed scheme ($\left|\Delta i^r_{dsh}{}^*\right|$ = 4.89A, 2.47A)

Fig. 18. Experiment B: Measurement of NI. (60r/min, rated current)

increased, current ripple is increased in load condition. And as discussed in section IV, $v_{qs,err}$ has DC component only in load condition. For this reason, generation of noise input is very small in load condition. This fact is reflected in Fig. 18. The waveforms of NI in both Fig. 18(a) and (b) are almost the same. The proposed scheme is more effective in no load and light load condition.

C. Improvement of Position Estimation Performance under Sensorless Drive

Fig. 19 shows the position estimation in the steady state. In the figure, conventional scheme indicates fixed voltage injection method explained in section II. And proposed scheme indicates the current ripple regulation and the computation of $\tilde{\theta}_{r,cal}$ in (18). In both cases, rms values of the current ripple are matched. Thanks to reduced NI, the position estimation under closed-loop sensorless operation has been improved. In case of the proposed scheme, rms value of position estimation error is decreased by 19.7% without increasing losses.

Fig. 20 shows the other experimental results. Under sensorless operation at 60r/min, torque command is jumped up to the rated value and return back to zero. The magnitude of the current ripple is kept uniform by the proposed scheme, while that varies depending on load condition by the conventional scheme. Due to the non-uniform magnitude of the current ripple, position estimation performance varies depending on load condition. In Fig. 20(a), 6th harmonic component in the estimated rotor position is quite relieved during the rated torque period. However, the position estimation performance is kept relatively consistent by the proposed scheme.

VII. Conclusions

In square wave voltage signal injection sensorless control, the injection voltage is distorted by voltage error induced by

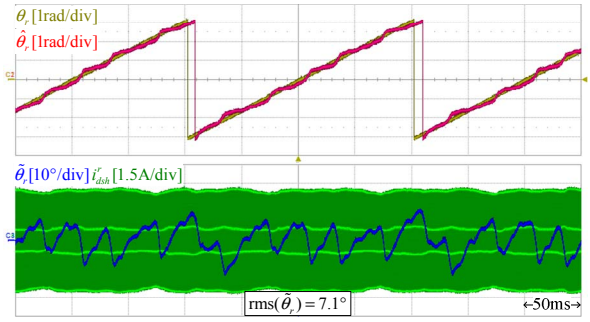

(a) Conventional scheme (V_h=11.5V)

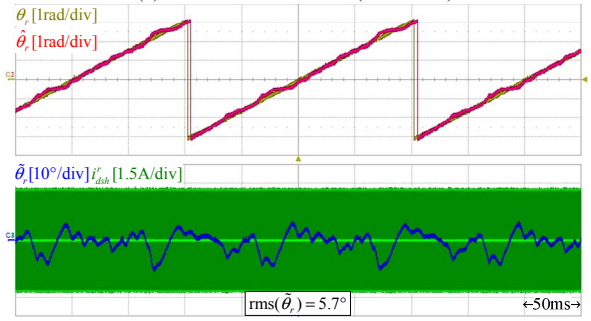

(b) Proposed scheme ($\left|\Delta i^r_{dsh}{}^*\right|$ =4A)

Fig. 19. Experiment C: Steady-state position estimation under sensorless drive. (60r/min, zero current)

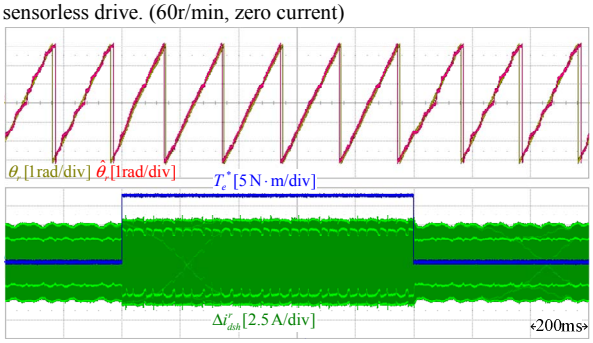

(a) Conventional scheme (V_h=11.5V)

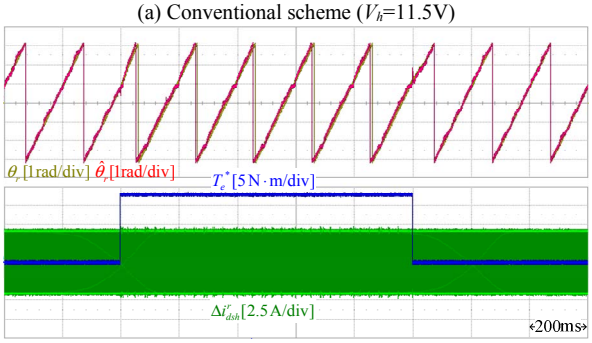

(b) Proposed scheme ($\left|\Delta i^r_{dsh}{}^*\right|$ =4A)

Fig. 20. Experiment C: Transient-state position estimation under sensorless drive. (60r/min)

the inverter nonlinearity effects. And the HF current ripple is also distorted. Since the position information is extracted from the HF current signal, the position estimation performance can be seriously degraded.

To improve this phenomenon, a voltage injection method which regulates the magnitude of the induced current ripple has been proposed. By the proposed method, the noise input in the position estimation has been reduced by 24.4% and 34.9% in no load condition depending on injection voltage. And the position estimation performance under sensorless operation was improved by 19.7% in no load condition.

REFERENCES

[1] T. Ohtani, N. Takada, and K. Tanaka, "Vector Control of Induction Motor without Shaft Encoder," *IEEE Trans. Ind. Appl.*, vol. 28, no. 1, pp. 157-164, Jan./Feb. 1992.

[2] J. Holtz, "Sensorless position control of induction motors-an emerging technology," *IEEE Trans. Ind. Electron*, vol. 45 no. 6, pp. 840 -851, Dec. 1998.

[3] P. L. Jansen and R. D. Lorenz, "Transducerless position and velocity estimation in induction and salient AC machines," *IEEE Trans. Ind. Appl.,* vol. 31, no. 2, pp. 240-247, Mar./ Apr. 1995.

[4] J. I. Ha, K. Ide, T. Sawa, and S. K. Sul, "Sensorless rotor position estimation of an interior permanent-magnet motor from initial states," *IEEE Trans. Ind. Appl.,* vol. 39, no. 3, pp. 761–767, May./Jun. 2003.

[5] Y. D. Yoon, S. K. Sul, Morimoto, K. Ide, "High-Bandwidth Sensorless Algorithm for AC Machines Based on Square-Wave-Type Voltage Injection," *IEEE Trans. Ind. Appl.*, vol. 47, no. 3, pp. 1361-1370, May./Jun. 2011.

[6] J. M. Guerrero, M. Leetmaa, F. Briz, A. Zamarron, and R. D. Lorenz, "Inverter nonlinearity effects in high-frequency signal-injection-based sensorless control methods," *IEEE Trans. Ind. Appl*., vol. 41, no. 2, pp. 618–626, Mar./Apr. 2005.

[7] C. Silva, G. M. Asher, and M. Sumner, "Influence of dead-time compensation on rotor position estimation in surface mounted PM machines using HF voltage injection," in *Proc. IEEE Power Conversion Conf.*, Osaka, Japan. pp. 1279–1284, 2002.

[8] J.-W. Choi and S.-K. Sul, "A new compensation strategy reducing voltage/current distortion in PWM VSI systems operating with low output voltages," *IEEE Trans. Ind. Appl.*, vol. 31, no. 5, pp. 1001–1008, Sept./Oct. 1995.

[9] J. W. Choi and S. K. Sul, "Inverter output voltage synthesis using novel dead time compensation," *IEEE Trans. Power Electron.*, vol. 11, no. 2, pp. 221–227, Mar. 1996

[10] N. Urasaki, T. Senjyu, T. Kinjo, T. Funabashi, and H. Sekine, "Dead time compensation for permanent magnet synchronous motor drive taking zero-current clamp and parasitic capacitance effects into account," *IEE Proc. Electric Power Appl.*, vol. 152, no. 4, pp. 845–853, Jul. 2005.

[11] Bon-Ho Bae, Seung-Ki Sul, "A compensation method for time delay of full-digital synchronous frame current regulator of PWM AC drive," *IEEE Trans. Ind. Appl*., vol. 39, no. 3, pp. 802–810, May 2003.

[12] Hyung-Min Ryu, Jung-Ik Ha, Seung-Ki Sul, Kozo Ide, Yoichi Yamamoto, Eiji Watanabe, "Compensation of Voltage Distortion in PWM-VSI by Prediction of Stator Currents at Switching Point," Conf. Rec. *of IEEJ, Annual Meeting*, vol.3, pp. 87-90. Apr. 1999.

[13] C. H. Choi and J. K. Seok, "Compensation of zero-current clamping effects in high-frequency-signal-injection-based sensorless PM motor drives," *IEEE Trans. Ind. Appl*., vol. 43, no. 5, pp. 1258–1265, Sept./Oct. 2007.

[14] K. Wiedmann, F. Wallrapp, and A. Mertens, "Analysis of inverter nonlinearity effects on sensorless control for permanent magnet machine drives based on high-frequency signal injection," in *Proc. 13th Eur. Conf. Power Electron. Appl.* (EPE), 2009, pp. 1–10.